With the improved design there is no need to control the total operation time t_0, while the time dependence of the voltage and flux can be optimized such that the time span of the manipulations τ is long enough to simplify time control and short enough to speed up the computation.

Also, the circuit of the current source, with resistance R_I, which couples the flux Φ_x to the SQUID by the mutual inductance M, introduces fluctuations and may destroy the coherence of the qubit dynamics. At the degeneracy point, the decoherence time is[21,22] $\tau_I = (1/\pi^3)(R_I/R_K)[\Phi_0^2/(E_J^0 M)]^2(\hbar/k_B T)$. This dephasing is slow if the current source is coupled weakly to the qubit (small M) and its resistance is high.

The control of the Josephson energies $E_J(\Phi_{xi})$ provides the possibility of coupling each selected pair of qubits, while keeping all the other ones uncoupled, bringing us close to the ideal model of equation (1). The simplest implementation of the coupling is to connect all N qubits in parallel with each other, and with inductor L (Fig. 3). Fast oscillations in the resulting LC-circuit produce an effective coupling of the qubits

$$\hat{H}_{\rm int} = -\sum_{i<j} \frac{E_J(\Phi_{xi})E_J(\Phi_{xj})}{E_L}\hat{\sigma}_y^i\hat{\sigma}_y^i \qquad (6)$$

where $E_L = [\Phi_0^2/(\pi^2 L)](C_J/C_{qb})^2$. The coupling shown in equation (6) can be understood as the magnetic energy of the inductor which is biased by a current composed of contributions from all qubits, $I^i \propto E_J^i\hat{\sigma}_y^i$.

With this design we can perform all gate operations. In the idle state the interaction hamiltonian of equation (6) is zero as all the Josephson couplings are turned off. The same is true during a one-qubit operation, as long as we perform one such operation at a time that is, only one $E_J^i \neq 0$. To perform a two-qubit operation with any given pair of qubits, say 1 and 2, E_J^1 and E_J^2 are switched on simultaneously, yielding the total hamiltonian $\hat{H} = -(E_J^1/2)\hat{\sigma}_x^i - (E_J^2/2)\sigma_x^2 - (E_J^1 E_J^2/E_L)\hat{\sigma}_y^1\hat{\sigma}_y^2$. Although not identical to equation (1), these two-bit gates, in combination with the single-bit operations discussed above, also provide a complete set of gates required for quantum computation.

To demonstrate that the constraints on the set of system parameters can be met by available technology, we suggest a suitable set. We choose junctions with capacitance $C_J = 300$ aF, corresponding to a charging energy (in temperature units) $E_C \approx 3$ K, and a smaller gate capacitance $C = 30$ aF to reduce the coupling to the environment (even lower C are available and improve the performance further). The superconducting gap has to be slightly larger, $\Delta > E_C$. Thus at a working temperature of the order of $T = 50$ mK, the initial thermalization is assured. We further choose $E_J^0 = 50$ mK; so the timescale of one-qubit operations is $\tau_{op} = \hbar/E_J \approx 70$ ps. Fluctuations associated with the gate voltages (equation (4)), with resistance $R_V \approx 50\,\Omega$, limit the coherence time to $\tau_V/\tau_{op} \approx 4{,}000$ operations. With the parameters of the flux-circuit $L_\Phi = 0.1$ nH, $M = 1$ nH and $R_I = 10^2$–$10^6\,\Omega$, current fluctuations have a weak dephasing effect. To assure fast two-bit operations, we choose the energy scale E_L to be of the order of $10E_J$, which is achieved for $L \approx 3\,\mu$H. With these parameters, the number of qubits in the circuit can be chosen in the range of 10–50, of course at the expense of shorter coherence times $\tau_{V,I}/N$.

Some further remarks are in order.

(1) After the gate operations, the resulting quantum state has to be read out. This can be achieved by coupling a normal-state single-electron transistor capacitively to a qubit. The important aspect is that during computation the transistor is kept in a zero-current state and adds only to the total capacitance. When the transport voltage is turned on, the phase coherence of the qubit is destroyed, and the dissipative current in the transistor, which depends on the state of the qubit, can be read out. This quantum measurement process has been described explicitly in ref. 16 by an analysis of the time-evolution of the density matrix of the coupled system.

(2) Inaccuracy in the control of fluxes, voltages and the time-span of operations leads to diffusion of the actual quantum state from the one that exists in the absence of errors[23]. A random error of order ϵ per gate limits the number of operations to a value which is of order ϵ^{-2}. For the circuit parameters above, $\epsilon = 1\%$ would lead to smaller effects than those produced by environment.

(3) Many powerful quantum algorithms make use of parallel operations on different qubits. Although this is not possible with the present system, it may be achievable by a more advanced design, making use of further tunable SQUIDs decoupling different parts of the circuit. Such modifications, as well as the further progress of nanotechnology, should provide longer coherence times and allow scaling to larger numbers of qubits. □

Received 16 October 1998; accepted 12 January 1999.

1. Lloyd, S. A potentially realizable quantum computer. *Science* **261,** 1569–1571 (1993).
2. Bennett, C. H. Quantum information and computation. *Phys. Today* **48**(10)**,** 24–30 (1995).
3. DiVincenzo, D. P. Quantum computation. *Science* **269,** 255–261 (1995).
4. Cirac, J. I. & Zoller, P. Quantum computations with cold trapped ions. *Phys. Rev. Lett.* **74,** 4091–4094 (1995).
5. King, B. E. *et al.* Demonstration of a fundamental quantum logic gate. *Phys. Rev. Lett.* **81,** 1525–1528 (1998).
6. Chuang, I. L., Gershenfeld, N. A. & Kubinec, M. Experimental implementation of fast quantum searching. *Phys. Rev. Lett.* **80,** 3408–3411 (1998).
7. Cory, D. G. *et al.* Experimental error correction. *Phys. Rev. Lett.* **81,** 2152–2155 (1998).
8. Jones, J. A., Mosca, M. & Hansen, R. H. Implementation of a quantum search algorithm on a quantum computer. *Nature* **393,** 344–346 (1998).
9. Turchette, Q. A., Hood, C. J., Lange, W., Mabuchi, H. & Kimble, W. Measurement of conditional phase shifts for quantum logic. *Phys. Rev. Lett.* **75,** 4710–4713 (1995).
10. Shnirman, A., Schön, G. & Hermon, Z. Quantum manipulations of small Josephson junctions. *Phys. Rev. Lett.* **79,** 2371–2374 (1997).
11. Averin, D. V. Adiabatic quantum computation with Cooper pairs. *Solid State Commun.* **105,** 659–664 (1998).
12. Bouchiat, V., Vion, D., Joyez, P., Esteve, D. & Devoret, M. H. Quantum coherence with a single Cooper pair. *Phys. Scripta T* **76,** 165–170 (1998).
13. Kane, B. E. A silicon-based nuclear spin quantum computer. *Nature* **393,** 133–137 (1998).
14. Loss, D. & DiVincenzo, D. P. Quantum computation with quantum dots. *Phys. Rev. A* **57,** 120–126 (1998).
15. Barenco, A. *et al.* Elementary gates for quantum computation. *Phys. Rev. A* **52,** 3457–3467 (1995).
16. Shnirman, A. & Schön, G. Quantum measurements performed with a single-electron transistor. *Phys. Rev. B* **57,** 15400–15407 (1998).
17. Rouse, R., Han, S. & Lukens, J. E. Observation of resonant tunneling between macroscopically distinct quantum levels. *Phys. Rev. Lett.* **75,** 1614–1617 (1995).
18. Maassen v.d. Brink, A., Schön, G. & Geerligs, L. J. Combined single-electron and coherent-Cooper-pair tunneling in voltage-biased Josephson junctions. *Phys. Rev. Lett.* **67,** 3030–3033 (1991).
19. Nakamura, Y., Chen, C. D. & Tsai, J. S. Spectroscopy of energy level spitting between two macroscopic quantum states of charge coherently superposed by Josephson coupling. *Phys. Rev. Lett.* **79,** 2328–2331 (1997).
20. Tinkham, M. *Introduction to Superconductivity* (McGraw-Hill, New York, 1996).
21. Leggett, A. J. *et al.* Dynamics of the dissipative two-state system. *Rev. Mod. Phys.* **59,** 1–85 (1987).
22. Weiss, U. *Quantum Dissipative Systems* (World Scientific, Singapore, 1993).
23. Miquel, C., Paz, J. P. & Zurek, W. H. Quantum computation with phase drift errors. *Phys. Rev. Lett.* **78,** 3971–3974 (1997).

Acknowledgements. We thank T. Beth, M. Devoret, D. P. DiVincenzo, E. Knill, K. K. Likharev and J. E. Mooij for discussions.

Correspondence and requests for materials should be addressed to Y.M. (e-mail: makhlin@tfp.physik.uni-karlsruhe.de).

Evidence against 'ultrahard' thermal turbulence at very high Rayleigh numbers

James A. Glazier*, Takehiko Segawa†, Antoine Naert‡ & Masaki Sano†

** Department of Physics, University of Notre Dame, Notre Dame, Indiana 46556–5670, USA*

† Research Institute of Electrical Communication, Tohoku University, 2-2-1 Katahira, Aoba-ku, Sendai 980, Japan

‡ Laboratoire de Physique, Ecole Normale Supérieure de Lyon, 46 Allée d'Italie, 69364 Lyon Cedex 7, France

Several theories[1–5] predict that a limiting and universal turbulent regime—'ultrahard' turbulence—should occur at large Rayleigh numbers (Ra, the ratio between thermal driving and viscous dissipative forces) in Rayleigh–Bénard thermal convection in a closed, rigid-walled cell. In this regime, viscosity becomes negligible, gravitationally driven buoyant plumes transport the heat

and the thermal boundary layer, where the temperature profile is linear, controls the rate of thermal transport. The ultrahard state is predicted to support more efficient thermal transport than 'hard' (fully developed) turbulence: transport efficiency in the ultrahard state grows as $Ra^{1/2}$, as opposed to $Ra^{2/7}$ in the hard state[6]. The detection of a transition to the ultrahard state has been claimed in recent experiments using mercury[7] and gaseous helium[8]. Here we report experiments on Rayleigh–Bénard convection in mercury at high effective Rayleigh numbers, in which we see no evidence of a transition to an ultrahard state. Our results suggest that the limiting state of thermal turbulence at high Rayleigh numbers is ordinary hard turbulence.

In thermal turbulence, several dimensionless numbers determine the degree of turbulence. The most important of these is the Rayleigh number, Ra, the ratio between thermal driving and viscous dissipation forces: $Ra = \alpha g \Delta T l^3/\kappa\nu$, where α is the coefficient of thermal expansion, κ the thermal conductivity, ν the kinematic viscosity, g the gravitational acceleration, l the typical length and ΔT the temperature difference across the cell. The second important quantity is the dimensionless velocity, the Reynolds number, Re, the ratio of shear forces to viscous forces: $Re = vl/\nu$, where v is a typical velocity. The fluid's Prandtl number, Pr, is the ratio between thermal and viscous dissipation: $Pr = \kappa/\nu$. Typical gases have $Pr \approx 1$, whereas $Pr > 1$ for most liquids) such as water and oil). The actual flow pattern of the fluid can be described in an averaged sense by the Nusselt number, Nu, the thermal transport efficiency, which is the ratio between gross thermal transport (including advection and diffusion) and diffusive thermal transport in the absence of flow. The larger Nu, the more efficient the convective thermal transport.

Convective thermal turbulence is inevitably anisotropic and non-homogeneous at large length scales. Two types of boundary layers are important. Near the container walls, flow velocity vanishes due to the no-slip condition which creates a highly sheared viscous boundary layer. The temperature profile becomes linear near the top and bottom walls, because only diffusion transports heat where advection is suppressed. The time-averaged temperature in the bulk is constant and equal to the average of the top and bottom plate temperatures due to strong mixing by the turbulent flow. The time-averaged profile is steep and linear in the thermal boundary layer. The thickness of the thermal boundary layer, which is the inverse of the temperature gradient, limits the gross heat transport across the turbulent cell. Thus Nu is proportional to the ratio between the cell height and the thickness of the thermal boundary layer.

The theories predicting $Nu \propto Ra^{1/2}$ make one of two assumptions. The first is that, because the thickness of the viscous boundary layer varies as $\sim Ra^{-1/2}$, it becomes negligible at very high Ra. Thus heat is advected by buoyant structures (for instance, plumes or thermals, rising masses of hot fluid or falling masses of cold fluid of classical mushroom-cloud shape) which move at the free fall velocity. That is, as viscous forces are negligible compared with inertial forces in this regime, the thermals accelerate as if they were free, undamped particles, subject to the buoyancy force produced by gravity. Because the free fall velocity, V scales as $\sim(\alpha g \Delta T l) \propto Ra^{1/2}$, the heat flux scales as $Nu \propto Ra^{1/2}$. The other argument is that when the viscous boundary layer becomes thinner than the thermal boundary layer (about $Ra = 10^{14}$ for He[9] and $Ra = 10^5$ for Hg[7,10]), the thickness of the viscous boundary layer limits the heat flux, which also gives $Nu \propto Ra^{1/2}$. The critical Ra for the transition, Ra_{crit}, is predicted to depend on the Prandtl number of the fluid as $Ra_{crit} \propto Pr^4$ (ref. 1). We emphasize that whereas Ra_{crit} depends on Pr and the particular cell geometry, both Kraichnan, and Shraiman and Siggia, claim that the existence of the transition should be universal and independent of these factors[1,3]. Extensive experiments by Wu have confirmed that scaling relations in turbulence are essentially independent of aspect ratio for aspect ratios above 1/2 (ref. 11). Shraiman and Siggia predict[1,2] $Ra_{crit} \approx 10^6$–10^8 for Hg[1,2]. Cioni *et al.* proposed[2] modifications to the theory which predicted $Ra_{crit} = 5 \times 10^5$ in Hg[7]. The Libchaber experiments[3,11–15] on turbulence in Rayleigh–Bénard convection in low temperature gaseous He found no indication of a shift in Nu scaling up to $Ra \approx 10^{14}$, but did see a suggestive change in the temperature power spectrum.

Because $Pr = 0.025$ at 20 °C in Hg compared to $Pr = 0.7$ for He gas below 1 atm at 5 K, searching for a new range in Hg required only a Ra number of the order of 10^8. Our initial Hg experiments used cylindrical cells, with aspect ratios of one-half, one, and two, to reach $Ra \approx 2 \times 10^9$. Our results were compatible with the hard turbulence Nu-versus-Ra scaling exponent of $2/7 = 0.285$ (ref. 16). The break in the data for an aspect ratio of two at $Ra \approx 2 \times 10^5$ results from a pattern competition instability in the flow[10]. For small $Ra \approx 10^6$–10^8, strong steady bulk mean flow in the cell of aspect ratio one reduces the measured scaling exponent to 0.25 (ref. 17). The exponent increases towards 2/7 with increasing Ra.

These measurements appear to invalidate both of the mechanisms proposed for the onset of ultrahard turbulence. The thermal and viscous boundary layers cross below $Ra \approx 10^5$, so we should definitely have seen the transition if the boundary crossing theory were correct. The boundary layer thickness argument also seems to fail: in Hg, after the onset of hard turbulence and when the viscous boundary layer crosses the thermal (above $Ra \approx 10^6$), our experiments have shown that both boundary layers shrink together with a nearly constant ratio and a scaling exponent of -0.20 ± 0.02, different from the theoretical value of $-1/2$ (ref. 17).

Cioni *et al.*[7], using a larger Hg cell of aspect ratio one, measured up to $Ra \approx 5 \times 10^9$. They claimed that the Nu-versus-Ra scaling exponent increased above 2/7 at a single point at the very top of their Ra range, but could not measure the new value. Chavanne *et al.*[8] studied Rayleigh–Bénard convection with an aspect ratio of one-half in gaseous and liquid He. In gas near the gas–liquid critical point they saw an increasing Nu-versus-Ra scaling exponent above $Ra \approx 10^{11}$ and measured an approximate power law of

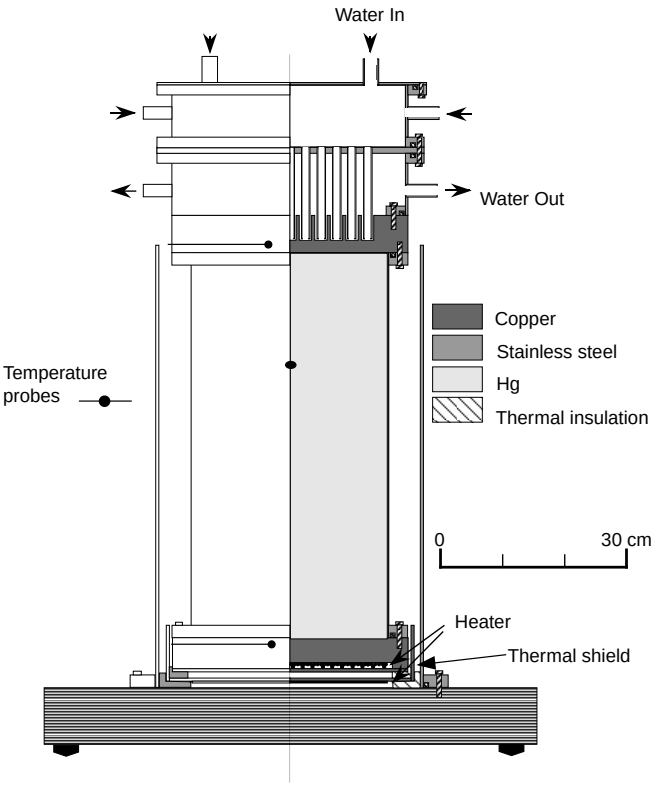

Figure 1 Schematic of the apparatus showing locations of bolometers.

$Nu \propto Pr^{0.072} Ra^{0.389 \pm 0.005}$. Chavanne *et al.* claimed that the new exponent was compatible with 1/2 scaling due to a logarithmic correction.

Our current experiment uses a cylinder of aspect ratio one-half (30 cm by 60 cm). We show the apparatus in Fig. 1. The top and bottom plates are solid copper 5 cm thick, coupled on top to cooling water via 212 vertical, thermally anchored cooling pipes. Heating is supplied by four resistance coils soldered to the bottom plate and driven by four regulated direct current power supplies (GP110-30x4, Takasago, Kawasaki, Japan) with an accuracy of 0.01% and a maximum combined heat supply of ~12,000 W. Cooling water is supplied by two building-type air-conditioning units (capacity ~20,000 W) with proportional-integral-derivative (PID) temperature regulation controlled by a flow-rate throttle. Temperature control of the top plate is accurate to 2% of the total temperature difference (ΔT) at the maximum power. Top-plate temperature ranges from 15 °C to 42 °C and bottom-plate temperature from 18 °C to 130 °C. The maximum variation of Prandtl number occurs at maximum power when it is 0.024 at the top plate and 0.018 at the bottom plate. The horizontal temperature non-uniformity across the plate diameter is much less than 1%. The size and power capacity were dictated by our need to search three decades higher in Ra than the highest value predicted for the transition, so that we could definitively determine whether the transition exists.

A thermal shield surrounds the cell. It can be temperature-matched to the cell to eliminate radiative and convective heat losses. Without the thermal shield, heat loss from the bottom plate is less than 1% at the highest Ra and much lower for smaller Ra. With the thermal shield, the worst case heat loss is less than 0.1%. Thermal conduction through the cell walls is negligible. The power supplied by the heater thus gives the heat flux to an accuracy of better than 1%. The temperature probes are semiconductor bolometers individually calibrated to an accuracy of better than 10^{-3} °C. Because the top- and bottom-plate temperature probes are embedded in the plates 1 cm from the copper–Hg interface, we must correct for the temperature drop across the copper. Temperature drops between the thermistor embedded in the bottom plate and the top surface of that plate, and between the bottom surface of the top plate and the thermistor embedded in this plate, are calculated from the applied heat flux and the thermal conductivity of the copper (401 J m^{-1} K^{-1}), and are used to correct the value of ΔT measured by the top and bottom thermistors. Ra and Nu are calculated using the corrected ΔT (ref. 17).

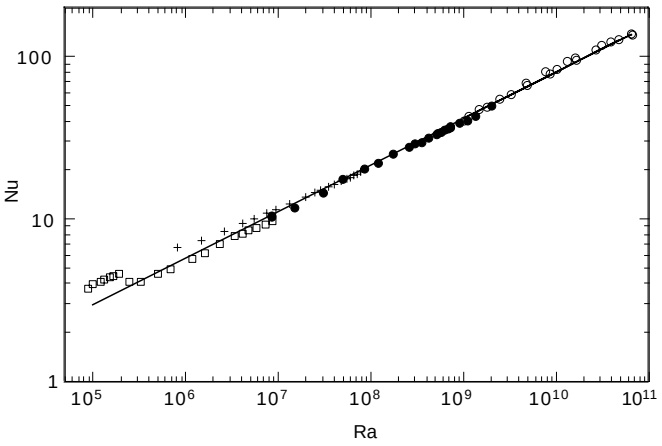

Figure 2 Nusselt number as a function of Rayleigh number. Open circles; aspect ratio = 0.5, large cell. Crosses; aspect ratio = 1, small cell. Squares; aspect ratio = 2, small cell. Filled circles; aspect ratio = 0.5, small cell. The solid line is $Nu \propto Ra^{0.285}$. The discontinuity in the data for aspect ratio = 2 is a result of a pattern competition instability. The reduced slope for small Ra for the data for an aspect ratio of one results from strong bulk circulation.

In Fig. 2 we show the Nu-versus-Ra curve for the combined data from our four experiments. From $Ra = 2 \times 10^5$ to 8×10^{10}, the Nusselt numbers lie on top of each other with a constant scaling exponent of 0.29 ± 0.01. This Rayleigh number is, to our knowledge, the highest yet achieved in thermal convection in a fluid of low Prandtl number, and the estimated Reynolds number is 5×10^5 (ref. 17), which is higher than that of Chavanne *et al.* Even at the highest Ra, our data show no indication of an increase in power law.

The Nu-versus-Ra curve is a highly averaged characterization of the fluid flow. In particular, transitions which change the temperature histograms and power spectra (which have never been observed) might not change the Nu-versus-Ra exponent. Figure 3 compares the power spectra and histograms for temperature time series taken for $Ra = 1.85 \times 10^9$ and $Ra = 5.14 \times 10^{10}$. The best fit to the scaling range of the temperature power-spectrum gives a slope of -1.47 ± 0.07. This slope and the range (less than five decades) is compatible with the result of Wu *et al.*[14] obtained for convective hard turbulence in helium. Except for the expected increase in inertial scaling range and the shrinking width of exponential decay in the temperature histogram, the two curves correspond exactly to each other. The small asymmetry in the histogram shape results from the location of the temperature probe above the centre of the cell, 15 cm from the cold top plate[10]. Again we see no sign of a qualitative change in the turbulence.

Chavanne *et al.*[8] clearly see an interesting effect in gaseous He—an increase of Nu at very high Ra—but the transition is gradual and never shows a clear power law, certainly not $Ra^{1/2}$. One complication in interpreting their results is that Pr changes rapidly near the critical point so that it is not constant from the top to the bottom of their cell. Although it is tempting to attribute this regime to ultrahard turbulence, it may instead be due to Pr effects, which partially mimic the predicted behaviour of ultrahard turbulence.

For our largest Ra, the Pr at the top plate (at $T = 130$ °C) is 0.018 and at the bottom plate $Pr = 0.024$ at $T = 42$ °C, a change of 35%. However the maximum Pr is 0.027, so viscous damping is always

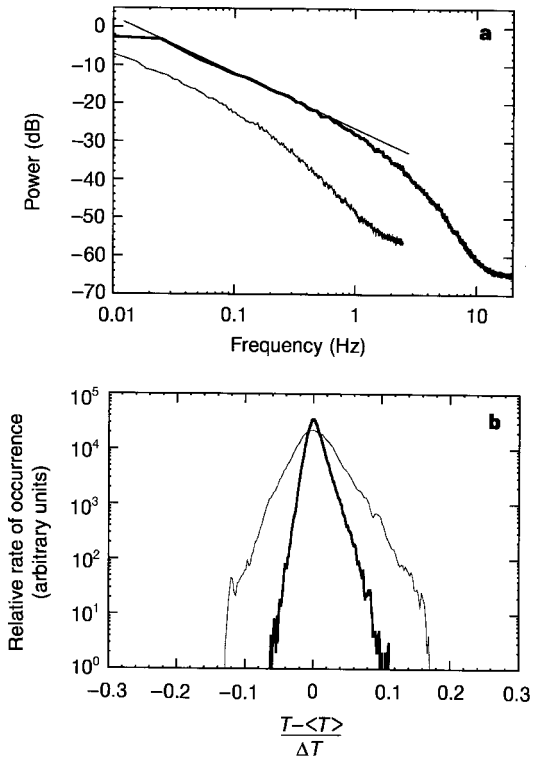

Figure 3 Temperature fluctuations data. **a**, Power spectra; **b**, histograms (thin line, $Ra = 1.85 \times 10^9$; thick line, $Ra = 5.14 \times 10^{10}$).

negligible. Thus the fundamental dissipation process remains the same and we expect the turbulence to be qualitatively unaffected by the Pr shift. In the He experiments the Pr shift is from 0.7 to 7 with the result that the primary dissipation mechanism shifts from thermal diffusion to viscous damping, for different locations within the same cell at a single Ra number.

In Hg, in which these complicating factors do not contribute (and for substantially higher Re), we see no evidence of a transition. Thus ultrahard turbulence may not exist. □

Received 17 July; accepted 29 December 1998.

1. Shraiman, B. I. & Siggia, E. D. Heat transport in high-Rayleigh-number convection. *Phys. Rev. A* **42,** 3650–3653 (1990).
2. Siggia, E. D. High Rayleigh number convection. *Annu. Rev. Fluid Mech.* **26,** 137–168 (1994).
3. Kraichnan, R. H. Turbulent thermal convection at arbitrary Prandtl number. *Phys. Fluids* **5,** 1374–1389 (1962).
4. Howard, L. N. Bounds on flow quantities. *Annu. Rev. Fluid Mech.* **4,** 473–494 (1972).
5. Busse, F. H. The optimum theory of turbulence. *Adv. Appl. Mech.* **18,** 77–121 (1978).
6. Castaing, B. *et al.* Scaling of hard thermal turbulence in Rayleigh-Bénard convection. *J. Fluid Mech.* **204,** 1–30 (1989).
7. Cioni, S., Ciliberto, S. & Sommeria, J. Strongly turbulent Rayleigh–Bénard convection in mercury: comparison with results at moderate Prandtl number. *J. Fluid Mech.* **335,** 111–140 (1997).
8. Chavanne, X. *et al.* Observation of the ultimate regime in Rayleigh–Bénard convection. *Phys. Rev. Lett.* **79,** 3648–3651 (1997).
9. Belmonte, A., Tilgner, A. & Libchaber, A. Temperature and velocity boundary layers in turbulent convection. *Phys. Rev. E* **50,** 269–279 (1994).
10. Segawa, T., Naert, A. & Sano, M. Matched boundary layers in turbulent Rayleigh–Bérnard convection of mercury. *Phys. Rev. E* **57,** 557–560 (1998).
11. Wu, X. Z. & Libchaber, A. Scaling relations in thermal turbulence: The aspect-ratio dependence. *Phys. Rev. A* **45,** 842–845 (1992).
12. Schewe, P. F. & Stein, B. One of the most convective fluids observed in the laboratory. *Physics News Update 342-1* (Am. Inst. Phys., 1997).
13. Heslot, F., Castaing, B. & Libchaber, A. Transition to turbulence in helium gas. *Phys. Rev. A* **36,** 5870–5873 (1987).
14. Wu, X. Z., Kadanoff, L., Libchaber, A. & Sano, M. Frequency power spectrum of temperature fluctuations in free convection. *Phys. Rev. Lett.* **64,** 2140–2143 (1990).
15. Wu, X. Z. & Libchaber, A. Non-Boussinesq effects in free thermal convection. *Phys. Rev. A* **43,** 2833–2839 (1991).
16. Takeshita,, T., Segawa, T., Glazier, J. A. & Sano, M. Thermal turbulence in mercury. *Phys. Rev. Lett.* **76,** 1465–1468 (1995).
17. Naert, A., Segawa, T. & Sano, M. High-Reynolds-number thermal turbulence in mercury. *Phys. Rev. E* **56,** 1302–1305 (1997).

Acknowledgements. J.A.G. was supported by the NSF and the ACS/PRF; M.S. acknowledges support from the Japanese Grant-in-Aid for Science Fund for the Ministry of Education, Science and Culture. Both are supported by the NSF-JSPS Cooperative Science Program.

Correspondence and requests for materials should be addressed to J.A.G. (e-mail: jglazier@rameau.phys.nd.edu).

Picosecond–milliångström lattice dynamics measured by ultrafast X-ray diffraction

Christoph Rose-Petruck*†, Ralph Jimenez*†, Ting Guo*, Andrea Cavalleri*, Craig W. Siders*, Ferenc Ráksi*†, Jeff A. Squier§, Barry C. Walker*†, Kent R. Wilson* & Christopher P. J. Barty‡

* *Department of Chemistry and Biochemistry,* ‡ *The Institute for Nonlinear Science,* § *Department of Electrical and Computer Engineering, The University of California, San Diego, La Jolla, California 92093–0339, USA*

Fundamental processes on the molecular level, such as vibrations and rotations in single molecules, liquids or crystal lattices and the breaking and formation of chemical bonds, occur on time-scales of femtoseconds to picoseconds. The electronic changes associated with such processes can be monitored in a time-resolved manner by ultrafast optical spectroscopic techniques[1], but the accompanying structural rearrangements have proved more difficult to observe. Time-resolved X-ray diffraction has the potential to probe fast, atomic-scale motions[2–5]. This is made possible by the generation of ultrashort X-ray pulses[6–10], and several X-ray studies of fast dynamics have been reported[6–8,11–15]. Here we report the direct observation of coherent acoustic phonon propagation in crystalline gallium arsenide using a non-thermal, ultrafast-laser-driven plasma—a high-brightness, laboratory-scale source of subpicosecond X-ray pulses[16–19]. We are able to follow a 100-ps coherent acoustic pulse, generated through optical excitation of the crystal surface, as it propagates through the X-ray penetration depth. The time-resolved diffraction data are in excellent agreement with theoretical predictions for coherent phonon excitation[20] in solids, demonstrating that it is possible to obtain quantitative information on atomic motions in bulk media during picosecond-scale lattice dynamics.

Crystalline gallium arsenide (GaAs) is available in large samples of very high crystalline quality, making it an ideal system for quantitative investigations using optical pumping and X-ray probing. Its physical parameters are known with great precision[21], and numerous prior studies[22] on its ultrafast electronic properties provide a solid foundation for interpretation, and for testing the potential of ultrafast X-ray diffraction. Indeed, some information on ultrafast lattice dynamics after optical excitation has already been indirectly inferred from a variety of linear and nonlinear optical techniques[22–24]. But owing to the short penetration depth of visible light, information on bulk dynamics in absorbing materials has not yet been obtained.

Figure 1 shows a schematic of our experiment. An ultrashort pulse of laser-generated Cu Kα X-rays (consisting of two closely spaced lines, $K\alpha_1$ and $K\alpha_2$) diffracts in a symmetric Bragg configuration from the 3.26-Å (111) lattice spacing in GaAs, penetrating ~2 μm into the bulk along the surface normal. A 30-fs pump pulse with variable time delay generates electron–hole pairs via interband excitation within the submicrometre penetration depth of the 800-nm light. By illuminating with light only a portion of the area probed by X-rays, we simultaneously observe the Kα lines from both photopumped and unperturbed areas of the semiconductor surface. Two-minute exposure X-ray-CCD images are normalized with respect to the incident X-ray flux and binned within the region of uniform illumination. In Fig. 2, the measured and calculated (described below) diffraction profiles are shown as a function of angular deviation from the Bragg angle, $\theta - \theta_B$, and of pump–probe time delay. Zero delay corresponds to the initial deviation of the diffracted signal. We observe for these early times that both of the original Kα lines broaden and shift slightly to larger angles (~20 arcsec), while two new lines appear, broader and weaker than the original lines and deviate by approximately −150 arcsec relative to the original Bragg angle. As the pump–probe delay is increased, these new lines decrease in width, increase in intensity, and merge asymptotically with the still broadened and shifted main lines. Finally, the angle-integrated diffraction signal (not shown) increases monotonically with delay, reaching a plateau of twice the unperturbed value.

The incident optical energy couples into the material by promoting electrons from the valence to the conduction band. Single- and two-photon (as well as free-carrier) absorption contribute to excitation during absorption of the pump pulse. Bandgap renormalization and state filling, not well characterized at these fluences, introduce additional nonlinearities to the excitation process. Also, efficient carrier diffusion at early times may smooth the energy deposition profile in a few picoseconds. After absorption, energy is transferred to the lattice via intraband relaxation[22] and delayed Auger heating[25]. Existing estimates of the Auger coefficient[26] in GaAs indicate that most of the energy is efficiently transferred to the lattice within a few picoseconds. X-ray diffraction, primarily sensitive to the acoustic phonon population, occurs only after the decay of the initially generated longitudinal optical phonons[22]. Following

† Present addresses: Department of Chemistry, Brown University, Providence, Rhode Island, USA (C.R.-P.); The Scripps Research Institute, La Jolla, California, USA (R.J.); IMRA America, Ann Arbor, Michigan, USA (F.R.); Department of Physics and Astronomy, the University of Delaware, Newark, Delaware, USA (B.C.W.).